Two-dimensional plasmonic polarons in *n*-doped monolayer MoS_2

Fabio Caruso,[1,2] Patrick Amsalem,[2] Jie Ma,[2] Areej Aljarb,[3] Thorsten Schultz,[2,4] Marios Zacharias,[5] Vincent Tung,[3] Norbert Koch,[2,4] and Claudia Draxl[2]

[1]*Institut für Theoretische Physik und Astrophysik, Christian-Albrechts-Universität zu Kiel, D-24098 Kiel, Germany*
[2]*Institut für Physik and IRIS Adlershof, Humboldt-Universität zu Berlin, Berlin, Germany*
[3]*Physical Sciences and Engineering Division, King Abdullah University of Science and Technology, Thuwal 23955-6900, Kingdom of Saudi Arabia*
[4]*Helmholtz-Zentrum für Materialien und Energie GmbH, Berlin, Germany*
[5]*Department of Mechanical and Materials Science Engineering, Cyprus University of Technology, P.O. Box 50329, 3603 Limassol, Cyprus*

(Received 6 July 2020; revised 16 May 2021; accepted 17 May 2021; published 27 May 2021)

We report experimental and theoretical evidence of strong electron-plasmon interaction in *n*-doped single-layer MoS_2. Angle-resolved photoemission spectroscopy measurements reveal the emergence of distinctive signatures of polaronic coupling in the electron spectral function. Calculations based on many-body perturbation theory illustrate that electronic coupling to two-dimensional carrier plasmons provides an exhaustive explanation of the experimental spectral features and their energies. These results constitute compelling evidence of the formation of plasmon-induced polaronic quasiparticles, suggesting that highly doped transition-metal dichalcogenides may provide a new platform to explore strong-coupling phenomena between electrons and plasmons in two dimensions.

DOI: 10.1103/PhysRevB.103.205152

I. INTRODUCTION

The interplay of charge confinement, reduced dielectric screening, and strong light-matter coupling in few-layer semiconducting transition-metal dichalcogenides (TMDCs) underpins a vast spectrum of emergent many-body effects, including the formation of excitons [1–4], trions [5], polarons [6,7], polaritons [8–12], and superconductivity [13]. At variance with three-dimensional solids, TMDCs further allow for unprecedented opportunities to tailor these phenomena via cavity embedding [14], circular dichroism [15,16], gating [13], nanostructuring [12,17], substrate engineering [18], and doping [6].

Highly tunable carrier densities are particularly desirable for the study of many-body interactions in TMDCs, as they may enable control of plasmons (collective excitation of the electron density) and polarons (electrons dressed by a phonon cloud) [19,20]. Polarons typically arise in semiconductors and insulators as a result of strong coupling to longitudinal-optical (LO) vibrational modes [19–22]. Polarons may lead to charge trapping [21,23] and to a renormalization of the band effective masses [22]. The relevance of such phenomena for the optoelectronic properties of solids, alongside the recent discovery of polarons in the photoemission spectrum of doped oxides [19,20] and two-dimensional (2D) materials [6,24], has reignited theoretical and experimental research on polaronic quasiparticles [7,21–23,25–28].

In close analogy to phonon-induced polarons, the formation of polaronic quasiparticles may also be stimulated by the coupling to extrinsic plasmons in highly doped semiconductors [25], leading to distinctive satellite features in angle-resolved photoemission spectroscopy (ARPES). The experimental observation of plasmonic polarons in three-dimensional solids is hindered by rather low electron-plasmon coupling strengths ($\lambda \leqslant 0.5$ [25]) and by the difficulty to achieve degenerate doping concentrations (a prerequisite for the excitation of plasmons) while simultaneously retaining crystallinity of the sample. Single-layer TMDCs circumvent this problem since highly tunable carrier densities can be realized. In particular, some of us recently demonstrated that the carrier population in the conduction band of monolayer MoS_2 and WS_2 can be tailored by stimulating the formation of chalcogen vacancies via repeated annealing cycles [29]. Additionally, we show here that the 2D confinement of plasmons and charge carriers provides suitable conditions for the establishment of a strong-coupling regime, leading to the emergence of plasmonic-polaron quasiparticles.

In this paper, we report the observation of plasmon-induced polarons in *n*-doped monolayer MoS_2. ARPES measurements of the conduction band reveal distinctive fingerprints of bosonic satellites due to electron-boson coupling. The satellite energy, ranging between 130 and 200 meV, is much larger than the characteristic phonon energies ($\hbar\omega < 60$ meV) and depends pronouncedly on the carrier density. These characteristics are incompatible with a coupling mechanism due to LO phonons. By explicitly accounting for the effects of electronic coupling to 2D plasmons in a first-principles many-body framework, our calculations of the spectral function identify electron-plasmon interactions as the origin of the polaronic spectral features observed in experiments. These findings

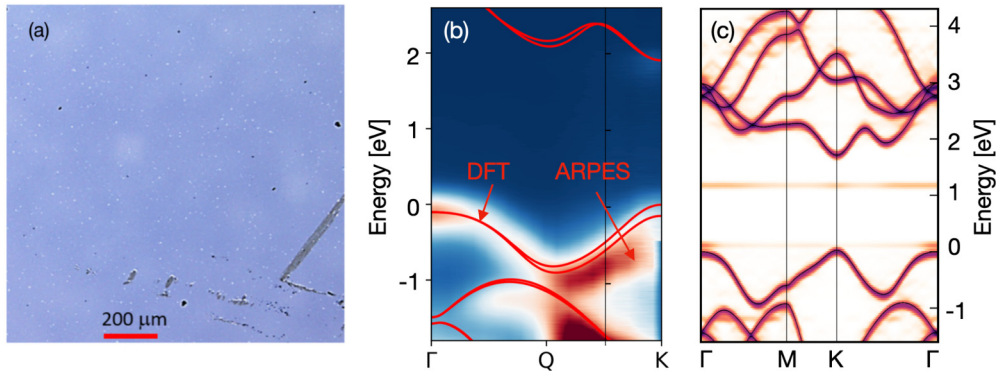

FIG. 1. (a) Optical micrograph of the monolayer MoS_2 samples on a sapphire substrate. (b) Experimental ARPES spectral function of n-doped monolayer MoS_2 on a sapphire substrate along the Γ-K path in the Brillouin zone. The DFT band structure for a freestanding MoS_2 monolayer is superimposed (red lines), where a scissor shift of 0.3 eV has been applied to the conduction band. The doping-induced population of the conduction band is reflected by the weak spectral intensity at K. (c) Spectral function of monolayer MoS_2 calculated using a $7 \times 7 \times 1$ supercell with one S vacancy. The DFT band structure of pristine monolayer MoS_2 is superimposed as a black line.

provide compelling evidence of the emergence of 2D plasmonic polarons in n-doped monolayer MoS_2, and they demonstrate the establishment of a strong-coupling regime resulting from the confinement of carriers and plasmons in two dimensions.

II. EXPERIMENT

A. Sample preparation and experimental setup

MoS_2 monolayer films with azimuthal disorder were grown by chemical-vapor deposition (CVD) on a sapphire substrate [30]. Top mechanical clamping of the sample enabled electrical contact of the monolayer to ground. Sample charging during ARPES measurements was avoided upon doping of the monolayer as described thereafter. Degenerate n doping was achieved by repeated *in situ* vacuum annealing cycles (with final annealing for 12 h at 850 K), which is known to effectively n dope a MoS_2 monolayer [31]. The low dimensionality of the system promotes the observation in the ARPES spectra of well-resolved electronic band dispersion along the high-symmetry directions Γ-K and Γ-M [32]. The optical micrograph reported in Fig. 1(a) indicates that the samples consist primarily of monolayer films with small multilayer seeds represented by the bright spots. The estimate doping concentrations $n_1 = 2.8 \times 10^{13}$ cm^{-2}, $n_2 = 4 \times 10^{13}$ cm^{-2}, and $n_3 = 5 \times 10^{13}$ cm^{-2} (referred to simply as n_1, n_2, and n_3 in the following) result from the formation of sulfur vacancies either by direct desorption of sulfur atoms or by desorption of substitutional oxygen present at sulfur-vacancy sites, naturally present in CVD-grown samples [33,34]. The Fermi-level position (corresponding to 0 eV binding energy) and the instrumental broadening were determined by fitting the Fermi edge of a gold polycrystal using a broadened Fermi-Dirac function. The photoemission measurements on n_1 and n_2 were performed at room temperature in an analysis chamber (base pressure of 2×10^{-10} mbar) equipped with a Specs Phoibos 100 hemispherical electron analyzer and using the He I radiation provided by monochromated helium discharge lamp (consisting of a HIS-13 lamp mounted on a VUV5046 UV monochromator). The overall energy resolution for n_1 and n_2 amounted to 117 meV (65 meV instrumental energy resolution) as determined from the Fermi edge of a polycrystalline gold sample, and the angular resolution was about $\pm 2^\circ$. The ARPES measurements on n_3 were performed at 230 K using a DA30-L hemispherical analyzer with an angular resolution of $\sim 0.3^\circ$ and an overall resolution of 100 meV (65 meV instrumental energy resolution). The energy distribution curves reported in Fig. 3 below were measured every 2° by rotating the manipulator about the polar axis.

B. ARPES measurements of n-doped MoS_2

Figure 1(b) illustrates ARPES measurements of the monolayer MoS_2 valence band along the Γ-Q-K high-symmetry line in the Brillouin zone for the doping concentration n_1. The presence of n-type carriers leads to the partial filling of the conduction-band bottom, as revealed by the finite spectral intensity measured at 2 eV in the vicinity of the K point. To verify that the vacancy concentration required to achieve population of the conduction band does not affect significantly the band dispersion of MoS_2, we performed band-structure calculations by explicitly accounting for the presence of sulfur vacancies. In particular, we computed the density functional theory (DFT) band structure for a $7 \times 7 \times 1 MoS_2$ supercell, from which a sulfur atom had been removed. This corresponds to a carrier density of 4.6×10^{13} cm^{-2}, and it is therefore representative of the largest impurity concentrations (n_2 and n_3) considered in this study. In order to compare it with the band structure of MoS_2 in the absence of vacancies, we subsequently unfolded the supercell band structure back to the first Brillouin zone of the pristine system using the unfolding techniques of Refs. [35,36] (see Appendix A). The spectral function of monolayer MoS_2 in the presence of sulfur vacancies obtained from this procedure is reported in Fig. 1(c), and it exhibits the emergence of nondispersive defect states slightly above the valence bands and about 0.6 eV below the conduction-band bottom. The comparison with the band structure of pristine MoS_2, superimposed as a black line in Fig. 1(c), suggests that, except for the emergence of in-gap defect states, band-structure renormalization effects due to the formation of sulfur vacancies are virtually negligible for the vacancy concentrations considered here.

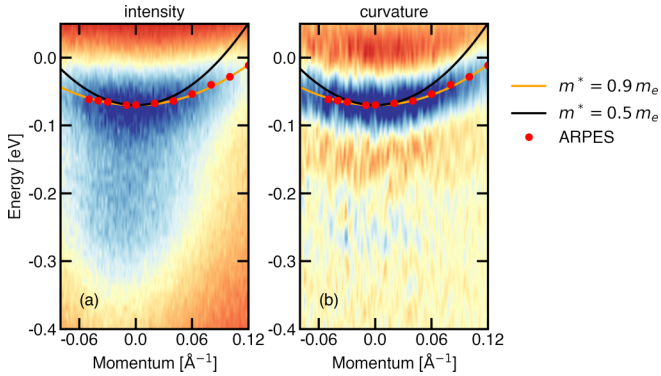

FIG. 2. (a) ARPES measurements of the conduction-band bottom of single-crystal monolayer MoS_2 and (b) curvature of the ARPES intensity. Crystal momentum is relative to the K high-symmetry point. Red dots indicate the quasiparticle peak position as determined from fitting the spectral function at selected momentum. Parabolic bands with effective mass values $m^* = 0.5m_e$ and $0.9m_e$ are included for comparison.

C. Measurements of the electron effective mass

In Fig. 2, we report ARPES measurements of the conduction-band bottom of single-crystal monolayer MoS_2 [Fig. 2(a)] and its curvature [Fig. 2(b)]. The red dots indicate the maximum ARPES intensity averaged in a momentum range of $\Delta k = 0.003$ Å^{-1}. Fitting a parabola to the dispersion, we obtain $m^* = 0.9m_e$. This value has been employed in all calculations of the electron-plasmon interaction reported below, and it is in good agreement with former experimental estimates [6,37]. Density functional theory calculations of the electron effective mass yield values ranging between $0.4m_e$ and $0.5m_e$ [38–41]. The effective mass obtained from our DFT calculations by fitting the conduction-band bottom is $m^* = 0.49m_e$, which is in good agreement with former DFT calculations. To rationalize the underestimation of DFT effective masses with respect to the experimental ones, we note that many-body effects due to electron-electron and electron-phonon interactions, which are known to strongly influence the effective mass, are not accounted for in the Kohn-Sham band structure as obtained from DFT. In particular, the electron-phonon interaction alone is expected to increase the *bare* DFT effective mass m^*_{DFT} to m^*_{ep} according to [42]

$$m^*_{\mathrm{ep}} = m^*_{\mathrm{DFT}}[1 + \lambda], \tag{1}$$

where λ is the electron-phonon coupling strength (also known as the "effective-mass renormalization parameter"). Recent helium-atom scattering experiments [43] estimated $\lambda \simeq 0.5$ for bulk MoS_2. Based on this value, one would expect a renormalization of the DFT effective $m^*_{\mathrm{DFT}} = 0.49m_e$ to $m^*_{\mathrm{ep}} = 0.73m_e$. Similarly, a quasiparticle description of band structure based on the *GW* approximation may also lead to an increase of the electron effective mass by up to 20%–30% with respect to DFT [44,45].

D. ARPES evidence of polaronic satellites

Figures 3(a) and 3(b) report ARPES spectral functions of monolayer MoS_2 for crystal momenta in the vicinity of the high-symmetry point K for doping concentrations n_1 and n_2, respectively. The on-curve labels indicate the photoelectron crystal momentum $\Delta\mathbf{k} = \mathbf{k} - \mathbf{k}_K$, relative to the K point in units of Å^{-1}. Energies are referenced to the Fermi level that is located 39 and 56 meV above the conduction-band minimum (CBM), respectively. At K and neighboring crystal momenta, the spectral functions are characterized by a quasiparticle peak close to the Fermi level. The peak position corresponds to the binding energy of quasi electrons around the CBM. At binding energies larger than those of quasiparticle excitations, the spectral function for carrier concentration n_1 (n_2) exhibits a shoulderlike structure redshifted by 130 meV (170 meV) from the quasiparticle peak and extending up to 0.6 eV below the Fermi level. These spectral features, indicated by arrows in Figs. 3(a) and 3(b), are visible exclusively in the vicinity of the K point and become more pronounced at higher carrier densities. These points suggest that the origin of these spectral features may not be attributed to in-gap defect states [illustrated in Fig. 1(c)], which are inherently nondispersive owing to their localized character.

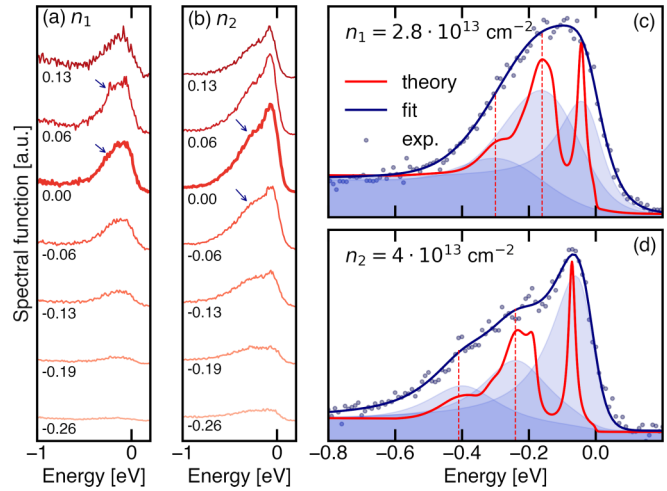

FIG. 3. (a) Spectral signatures of plasmonic polarons in the ARPES spectral function of n-doped monolayer MoS_2 for carrier densities (a) $n_1 = 2.8 \times 10^{13}$ and (b) $n_2 = 4 \times 10^{13}$ cm^{-2}. Labels indicate the photoelectron crystal momentum relative to the K point ($\Delta\mathbf{k} = \mathbf{k} - \mathbf{k}_K$) along K-Γ in units of Å^{-1}, and satellite features are indicated by arrows. Energies are relative to the Fermi level. ARPES measurements (dots) and first-principles calculations (red) of the spectral function at K for (c) n_1 and (d) n_2. Vertical dashed lines mark the positions of the first and second satellite peaks in the calculated spectra. The fit (dark blue) of the experimental spectra and its spectral decomposition as Gaussian line shapes (shaded curves) are guides to the eye.

A more detailed view of these spectral signatures is given in Figs. 3(c) and 3(d), which report the spectral functions for n_1 and n_2 [corresponding to the thick lines in Figs. 3(a) and 3(b)]. For n_2, the spectral function exhibits a satellite structure at 170 meV and a less pronounced secondary structure at 330 meV below the quasiparticle peak. To better resolve the underlying spectral features that give rise to the satellite, in Fig. 4 we apply the prescription of Ref. [46] and deconvolute the experimental spectra by a Gaussian function to reduce the spectral broadening due to finite resolution and

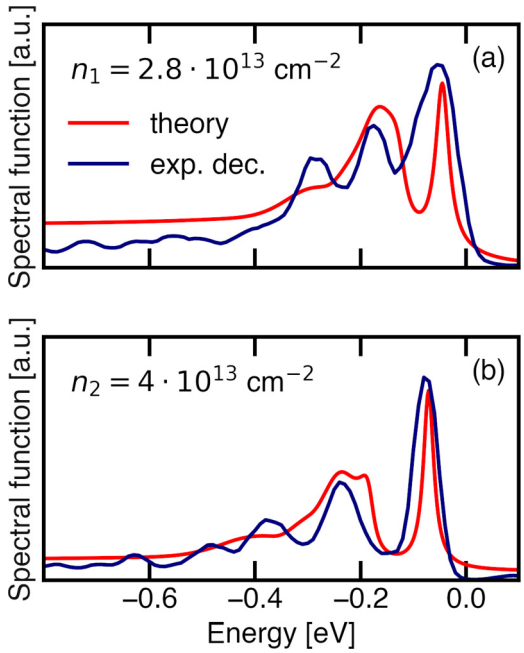

FIG. 4. Comparison between the calculated spectral function (theory) and the deconvoluted experimental spectrum (exp. dec.) for (a) $n_1 = 2.8 \times 10^{13}$ and (b) $n_2 = 4 \times 10^{13}$ cm^{-2}. To approximately remove the finite broadening due to finite-resolution effects, the experimental data have been deconvoluted with a Gaussian function with full width at half maximum of 137 and 198 meV, respectively, following the prescription of Ref. [46].

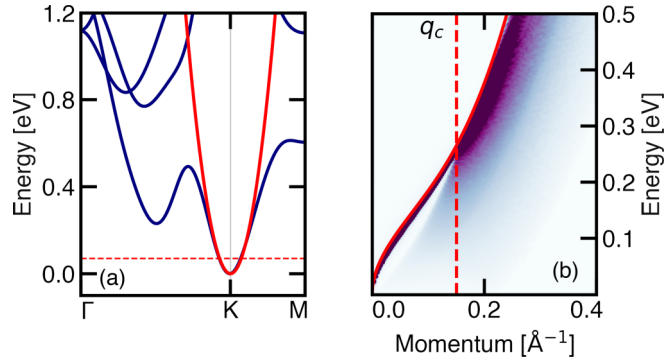

FIG. 5. (a) Conduction band of monolayer MoS_2 obtained from density-functional theory (blue) and dispersion of a 2D homogeneous electron gas with effective mass $m^*_{\mathrm{DFT}} = 0.49$ (red). The dashed horizontal lines mark the position of the Fermi level ϵ_{F} for the carrier concentration n_2. Energies are referenced to the conduction-band minimum. (b) Loss function and plasmon dispersion of n-doped MoS_2 for the carrier concentration n_2. The vertical dashed line marks the critical momentum cutoff $\mathbf{q}_c$ corresponding to the onset of Landau damping for 2D plasmons. The solid line illustrates the plasmon dispersion.

lifetime effects. These spectral features closely resemble the characteristic spectral fingerprints of electron-boson interaction in photoemission spectroscopy. Specifically, (i) they have nonvanishing intensity within the gap and therefore may not be attributed to the emission of a photoelectron, and (ii) they are roughly spaced from the quasiparticle peak by multiples of $\hbar\Omega = 130$, 170, and 200 meV for n_1, n_2, and n_3, respectively, as illustrated by the spectral-function decomposition in terms of Gaussian line shapes shown in Figs. 3(c) and 3(d). These points suggest that carriers in the conduction band may be subject to polaronic coupling to bosonic excitations, such as polar phonons or 2D carrier plasmons, and that the first and second satellites may stem from the excitation of one and two bosons with an effective energy $\hbar\Omega$ alongside the creation of a photohole.

The comparison between the boson energy $\hbar\Omega$ and the energy of optical phonons in monolayer MoS_2, which ranges between 30 and 60 meV [47], allows us to promptly exclude the Fröhlich interaction between electrons and LO phonons as a possible coupling mechanism responsible for the satellite formation. Recent experimental and theoretical investigations of *bulk* MoS_2 [6,7] have, indeed, revealed the emergence of Holstein polarons in ARPES. However, their spectral signatures occur at 30–40 meV below the Fermi level, energies that are too small to possibly explain the polaronic spectral features of Fig. 3. In analogy to polarons in oxides [27], strong coupling between electrons and plasmons may also trigger the formation of plasmon-induced polaronic quasiparticles (*plasmonic polarons*) in n-doped semiconductors and insulators [25,26]. Plasmonic polarons result from the simultaneous excitation of a plasmon and a hole, and they manifest themselves in ARPES under the form of photoemission satellites. To inspect whether a bosonic coupling mechanism induced by carrier plasmons may account for these phenomena, we proceed to investigate electron-plasmon interactions in doped MoS_2.

III. THEORY

A. Dispersion and density of states of 2D plasmons

For concentrations of n-type carriers larger than 1×10^{13} cm^{-2}, MoS_2 undergoes a metal-insulator transition [48], characterized by the onset of metallic transport properties [49] and by the partial filling of the K valley in the conduction band. The conduction-band dispersion of monolayer MoS_2 as obtained from density functional theory calculations is reported in Fig. 5(a). The Fermi energy of the doped system depends linearly on the carrier concentration n via the expression $\epsilon_{\mathrm{F}} = \pi\hbar^2 n/m^* N_{\mathrm{v}} - E_{\mathrm{CBM}}$, with $N_{\mathrm{v}} = 2$ being the K-valley degeneracy and E_{CBM} being the energy of the CBM. For the experimentally determined Fermi energies $\epsilon_{\mathrm{F}} = 39$, 56, and 70 meV, this expression allows one to determine carrier concentrations n_1, n_2, and n_3, respectively. For n_2, the Fermi energy is marked by the horizontal dashed line in Fig. 5(a). Upon interaction with light, extrinsic carriers in the conduction band can be collectively excited, leading to well-defined 2D carrier plasmon resonances. The energy-momentum dispersion relation of 2D plasmons in MoS_2 is here approximated by the loss function $L(\omega) = \mathrm{Im}\,[\epsilon(\mathbf{q}, \omega)]^{-1}$ of a 2D homogeneous electron gas [50,51]. All calculations have been conducted using the experimental effective mass $m^*_{\mathrm{exp}} = 0.9 m_{\mathrm{e}}$ determined above. The influence of m^* on the calculations and on electron-plasmon interaction is discussed in Appendix B. We further explicitly account for the extrinsic dielectric environment induced

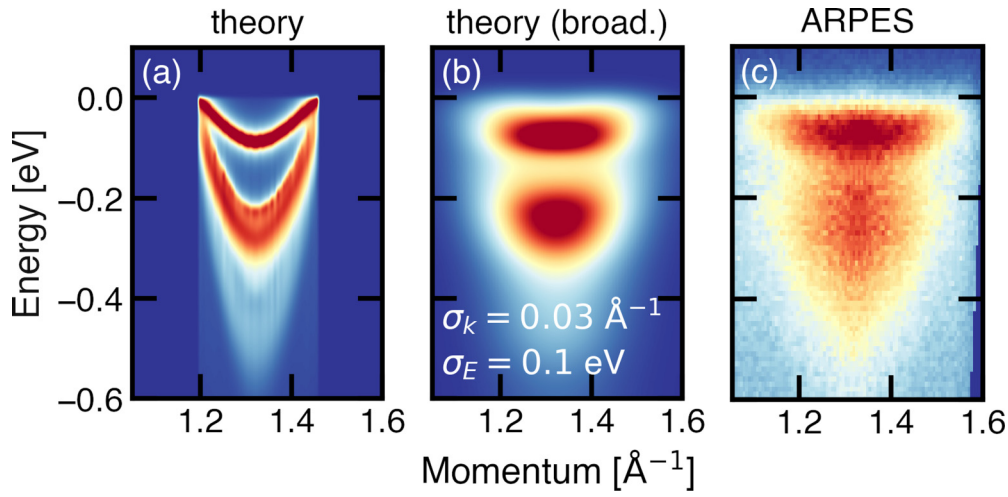

FIG. 6. (a) First-principles calculations of the angle-resolved spectral function of MoS_2 at K for a carrier concentration $n_3 = 5 \times 10^{13}$ cm^{-2}. (b) Influence of finite energy and momentum resolutions on the angle-resolved spectral function. (c) ARPES measurements.

by the semi-infinite sapphire (Al_2O_3) substrate by introducing the dielectric constant $\epsilon_\infty^S = (1 + \epsilon_\infty^{Al_2O_3})/2 = 6.3$, with $\epsilon_\infty^{Al_2O_3} \simeq 11.6$ being the high-frequency dielectric constant of bulk sapphire [52].

The loss function, illustrated in Fig. 5(b) for the carrier concentration n_2, exhibits pronounced plasmon peaks, with plasmon energies $\hbar\omega_{pl}(\mathbf{q})$ ranging from 0 to 0.24 eV. Only plasmons with momenta $|\mathbf{q}| < q_c$ can be excited, where $q_c \simeq 0.15$ Å^{-1} [marked by a dashed vertical line in Fig. 5(b)] is the critical momentum for the onset of Landau damping, namely, the decay of plasmons upon excitation of electron-hole pairs. The plasmon dispersion obtained from the loss function compares well with the analytical result for homogeneous 2D metals $\omega_{\mathbf{q}}^{pl} = F(q)\sqrt{2\pi nq/m^*\epsilon_\infty^S}$ [53], illustrated in Fig. 5(b) as a solid line. Here, $F(q) = (1 + q/2\kappa)[(1 + q/2\kappa)^{-1} + q^3 N_v/(4\pi n\kappa)]^{\frac{1}{2}}$ and $\kappa = 2m^*/\epsilon_\infty^S$.

In systems characterized by electronic coupling to weakly dispersive bosonic modes (e.g., optical phonons and three-dimensional plasmons) the energy of polaronic satellites can be directly related to the boson energy. Therefore, at first sight it might seem surprising that the coupling to 2D plasmons could give rise to a satellite peak with well-defined energy since the 2D plasmon dispersion continuously spans the energy range between 0 and 240 meV [Fig. 5(b)]. To clarify this aspect, we show in the following that the satellite energy is related to the average energy of 2D plasmons in the Brillouin zone. This finding leads us to the interpretation of the measured ARPES satellite as a result of the collective coupling to all 2D plasmons in the system, rather than to a single bosonic excitation. To estimate the average energy of 2D plasmons, we consider the density of states of plasmonic excitations:

$$J(\omega) = \Omega_{BZ}{}^{-1} \int_{\Omega_{BZ}} d\mathbf{q}\,\delta\left(\omega - \omega_{\mathbf{q}}^{pl}\right) = \kappa\omega^3\theta(\omega_c - \omega), \quad (2)$$

where $\kappa = (m^*\epsilon_\infty^S)^2(\pi\Omega_{BZ}n^2)^{-1}$ and $\omega_c = \omega_{\mathbf{q}_c}^{pl}$ is the plasmon energy at the critical momentum $\mathbf{q}_c$. This result may be promptly verified by analytical integration of Eq. (2), as illustrated in Appendix D. For n_1, n_2, and n_3, the density of states $J(\omega)$ is illustrated in Fig. 10. From Eq. (2), we can estimate the average plasmon energy as $\hbar\overline{\omega} = \hbar\int J(\omega)\omega d\omega[\int J(\omega)d\omega]^{-1} = 4\hbar\omega_c/5$ and the standard deviation $\sigma = \hbar(\overline{\omega^2} - \overline{\omega}^2)^{1/2} \simeq 0.45\hbar\omega_c$. For n_2, the value $\hbar\omega_c \simeq 0.24$ eV yields $\hbar\overline{\omega} = 190$ meV, which agrees well with the effective boson energy $\hbar\Omega = 170$ meV derived from the satellite energy. Similarly, the spread of the plasmon energies in the Brillouin zone is quantified by $2\sigma = 80$ meV, which is in good agreement with the half-width at half maximum of the satellite peak $\Delta w = 90$ meV, which we extract from Gaussian decomposition of the experimental spectra. This analysis suggests that the observation of a well-defined satellite in ARPES is compatible with a bosonic coupling mechanism induced by 2D carrier plasmons. In particular, the satellite energy can be related to the average energy $\hbar\overline{\omega}$ of 2D plasmons, whereas the satellite linewidth reflects the spread of plasmon energies as quantified by the standard deviation σ.

B. First-principles description of 2D plasmonic polarons in ARPES

To quantitatively demonstrate the influence of the electron-plasmon interaction on ARPES measurements, we conducted first-principles calculations of the spectral function based on the cumulant expansion approach [54–57], the state of the art for spectral-function calculations of coupled electron-boson systems [58–60]. The cumulant spectral function can be expressed as [22]

$$A(\mathbf{k}, \omega) = \sum_n e^{A_{n\mathbf{k}}^S(\omega)*} A_{n\mathbf{k}}^{QP}(\omega), \quad (3)$$

where $*$ denotes convolution over frequency and $A_{n\mathbf{k}}^{QP}(\omega) = 2\pi^{-1}\mathrm{Im}\,[\hbar\omega - \varepsilon_{n\mathbf{k}} - \Sigma_{n\mathbf{k}}(\varepsilon_{n\mathbf{k}})]^{-1}$ is the quasiparticle contribution to the spectral function. $\varepsilon_{n\mathbf{k}}$ is the single-particle energy, and Σ is the electron self-energy due to the electron-plasmon interaction [61]. The electron-plasmon self-energy accounts explicitly for the coupling to 2D plasmons via the coupling matrix elements introduced in Appendix C. Dynamical correlations due to the electron-plasmon interaction are

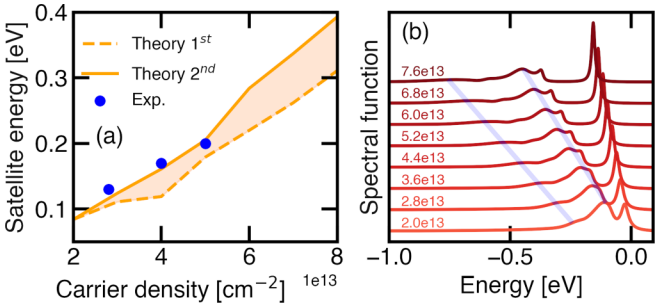

FIG. 7. (a) Dependence on the carrier density of the measured (dots) and calculated satellite energy (shaded area). The satellite energies are relative to the quasiparticle peak. (b) Calculated electron-plasmon spectral functions of MoS_2 at the K high-symmetry point for several carrier concentrations (in cm^{-2}). Energies are relative to the Fermi level, and the blue lines are a guide to the eye.

accounted for by the satellite function $A^{\mathrm{S}}_{n\mathbf{k}}$:

$$A^{\mathrm{S}}(\omega) = \frac{\beta(\omega) - \beta(\varepsilon/\hbar) - (\omega - \varepsilon/\hbar)(\partial\beta/\partial\omega)|_{\varepsilon/\hbar}}{(\hbar\omega - \varepsilon)^2}, \qquad (4)$$

with $\beta(\omega) = \frac{1}{\pi}\mathrm{Im}\,\Sigma(\varepsilon/\hbar - \omega)\theta(\mu/\hbar - \omega)$, and the dependence on n and $\mathbf{k}$ has been omitted [62].

The cumulant spectral function of n-doped MoS_2 is illustrated in Figs. 3(c)–3(d) as a red line for n_1 and n_2, respectively. The experimental background signal has been added to theoretical data to facilitate the comparison. The calculated spectral function exhibits two distinct satellite resonances at energies in excellent agreement with the ARPES spectral features. The Taylor expansion of Eq. (3) up to second order in A^{S} promptly reveals the physical origin of these spectral features: besides the quasiparticle peak, arising from A^{QP} alone, the second term in the expansion stems from the convolution $A^{\mathrm{S}} * A^{\mathrm{QP}}$, and its intensity may be attributed to the rate of photoemission processes resulting from the coupled excitation of a photohole and a plasmon. Similarly, subsequent arguments in the Taylor expansion can be related to multiple plasmon excitations. This allows us to relate subsequent satellites to photoemission processes resulting from the simultaneous excitation of a photohole and emission of plasmons. The quantitative agreement between experiment and theory is further illustrated in Fig. 6, where the full calculated and measured angle-resolved spectral functions are compared for the carrier concentration $n_3 = 5 \times 10^{13}$ cm^{-2}. Finite experimental resolution for energy (momentum) is explicitly accounted for in Fig. 6(b) by convolution with a Gaussian function with full width at half maximum of 100 meV (0.03 $Å^{-1}$). The calculated satellite structure is sharper than the measurements since our calculations do not explicitly account for finite lifetime effects in the plasmon dispersion arising from the plasmon-phonon scattering. Scattering between plasmons and phonons can, indeed, lower the plasmon lifetime, introducing additional broadening of the plasmon satellite [51].

Finally, in Fig. 7(a) we compare the dependence of the satellite energy on the carrier concentration, as obtained from experiments and theory. The dashed and solid lines denote the energy of the first and second substructures of the satellite peak, respectively, extracted from the electron-plasmon spectral functions illustrated in Fig. 7(b). Remarkably, the increase of the satellite energy with carrier concentration is in excellent agreement with the calculated trend, further corroborating the plasmonic origin of the photoemission satellites.

IV. CONCLUSIONS

In conclusion, we reported the observation of 2D plasmonic polarons in n-doped monolayer MoS_2 at degenerate doping concentrations. The emergence of distinctive signatures of polaronic satellites in ARPES experiments provides compelling evidence of the strong coupling between 2D carrier plasmons and extrinsic carriers, and it is corroborated by first-principles calculations of the electron-plasmon interaction. This finding indicates that, at sufficiently large doping concentrations, the quantum confinement of holes and plasmons in a 2D semiconductor triggers the onset of a strong-coupling regime, whereby electron-plasmon coupling results in the formation of 2D plasmonic polarons.

ACKNOWLEDGMENTS

This work was funded by the Deutsche Forschungsgemeinschaft (DFG), Projects No. 182087777 (SFB 951) and No. 443988403. F.C. acknowledges useful discussions with P. Pavone. A.A. and V.T. are indebted to the KAUST Office of Sponsored Research (OSR) for support under Award No. OSR-2018-CARF/CCF-3079. M.Z. acknowledges support from the program METAΔIΔAKTΩP of the Cyprus University of Technology and the DECI resource Saniyer at UHeM based in Turkey [63] with support from the PRACE aisbl.

APPENDIX A: BAND-STRUCTURE CALCULATIONS WITH SULFUR VACANCIES

The band structure of monolayer MoS_2 in the presence of a sulfur vacancy in a $7 \times 7 \times 1$ supercell [corresponding to a carrier density $n = 4.6 \times 10^{13}$ cm^{-2} and illustrated in Fig. 1(c)] has been obtained from the evaluation of the electron spectral function using the zone unfolding technique [35,64], as implemented for plane waves in Ref. [36]. The procedure is based on the calculation of the electron spectral function in the Lehmann representation, which reflects the momentum-resolved density of states. It is given by

$$A_{\mathbf{k}}(\varepsilon) = \sum_{m\mathbf{K}} P_{m\mathbf{K},\mathbf{k}}\,\delta[\varepsilon - \varepsilon_{m\mathbf{K}}]. \qquad (A1)$$

Here, the summation runs over the bands m and wave vectors $\mathbf{K}$ defining the Kohn-Sham state $|\psi^{\mathrm{v}}_{m\mathbf{K}}\rangle$ with energy $\varepsilon_{m\mathbf{K}}$, calculated in the $7 \times 7 \times 1$ MoS_2 supercell with one S vacancy. The quantity $P_{m\mathbf{K},\mathbf{k}}$ represents the spectral weight, defined by

$$P_{m\mathbf{K},\mathbf{k}} = \sum_{n} \left|\langle\psi^{\mathrm{v}}_{m\mathbf{K}}|\psi_{n\mathbf{k}}\rangle\right|^2, \qquad (A2)$$

which corresponds to the transition probability between $|\psi^{\mathrm{v}}_{m\mathbf{K}}\rangle$ and $|\psi_{n\mathbf{k}}\rangle$, evaluated in the unit cell of pristine monolayer MoS_2. Following the procedure of Ref. [36], we evaluate $P_{m\mathbf{K},\mathbf{k}}$ using only the plane wave expansion of the states in the supercell containing the vacancy. We select a set of 158 $\mathbf{K}$

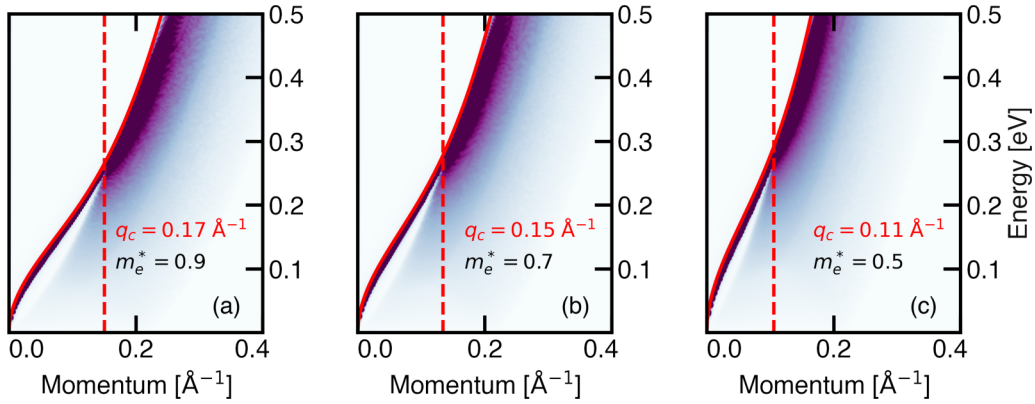

FIG. 8. Dispersion of 2D plasmons for a carrier concentration $n = 4 \times 10^{13}$ cm^{-2} with effective masses (a) $m^* = 0.9m_e$, (b) $m^* = 0.7m_e$, and (c) $m^* = 0.5m_e$.

points that are mapped onto equally spaced **k** points along the Γ-*K*-*M*-Γ path in the Brillouin zone of the unit cell. The one-by-one mapping is performed via a reciprocal lattice vector of the structure with the vacancy. For each **K** point we calculate $P_{m\mathbf{K},\mathbf{k}}$ and $\varepsilon_{m\mathbf{K}}$ and eventually obtain the spectral function $A_{\mathbf{k}}(\varepsilon)$ along the full path, as shown in Fig. 1(c).

APPENDIX B: DEPENDENCE OF THE ELECTRON-PLASMON INTERACTION ON THE EFFECTIVE MASS

All calculations reported in this paper have been conducted using the experimental effective mass $m^* = 0.9m_e$. In the following, we discuss the influence of this parameter on the plasmon dispersion and on the spectral signatures of the electron-plasmon interaction.

In Figs. 8(a)–8(c), we report the dispersion of 2D plasmons calculated using $m^* = 0.9m_e$, $m^* = 0.7m_e$, and $m^* = 0.5m_e$, respectively, for a carrier concentration $n = 4 \times 10^{13}$ cm^{-2}. The dispersion of 2D plasmons becomes more pronounced for smaller values of the effective mass. This behavior can be easily understood from the dependence of the plasmon energy $\hbar\omega_{\mathbf{q}}$ on $(m^*)^{-1/2}$ which follows from the plasmon dispersion relation $\hbar\omega_{\mathbf{q}} = \sqrt{2\pi nq/\epsilon_\infty m^*}$. A smaller m^* further entails a more dispersive band and thus a lower value of the critical momentum q_c at which 2D plasmons become degenerate with the energy of electron-hole pairs. Correspondingly, the plasmon dispersion covers virtually the same energy range for both values of the effective mass. Based on these considerations, one may expect the energy of the plasmon satellites to be only marginally affected by changes in the effective mass.

To explore this aspect on quantitative grounds, we report in Figs. 9(a)–9(c) the electron spectral function due to the electron-plasmon interaction evaluated for $m^* = 0.5m_e$, $0.7m_e$, and $0.9m_e$, respectively. A smaller value of the electron effective mass results in a lowering of the satellite peak intensity. The origin of this behavior can be attributed to the lower plasmonic density of states which, in turn, underpins a reduced electron-plasmon coupling strength. Remarkably, the satellite energy is only marginally affected, and it remains in good agreement with the energy range covered by the satellite spectral features observed in ARPES measurements.

In summary, these results indicate that while a change in the effective mass may influence the intensity of 2D plasmon satellites, it does not significantly influence the energy range covered by the satellite, and therefore, it does not affect the validity of our findings.

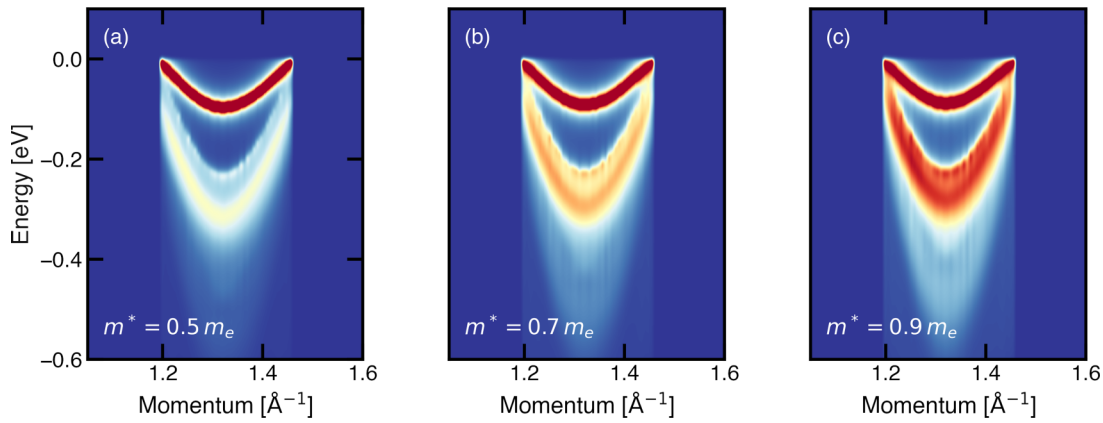

FIG. 9. Calculated spectral function of monolayer MoS_2 due to the electron-plasmon interaction for a carrier concentration $n = 5 \times 10^{13}$ cm^{-2} and for several values of the electron-effective mass parameter: (a) $m^* = 0.5m_e$, (b) $0.7m_e$, and (c) $0.9m_e$.

APPENDIX C: ELECTRON-PLASMON COUPLING FROM FIRST PRINCIPLES

In the following, we discuss how formalism of electron-plasmon coupling [65,66] can be adapted to investigate electron-plasmon interactions in a doped 2D semiconductor. The coupling matrix elements are given by

$$g^{\mathrm{e-pl}}_{mn}(\mathbf{k},\mathbf{q}) = \left(\frac{4\pi}{\Omega_{\mathrm{BZ}}}\right)^{\frac{1}{2}} \left[\frac{\partial\epsilon(\mathbf{q},\omega)}{\partial\omega}\right]^{-\frac{1}{2}}_{\omega^{\mathrm{pl}}_{\mathbf{q}}} \frac{1}{|\mathbf{q}|} M_{\mathbf{G}=0}(\mathbf{k},\mathbf{q}). \tag{C1}$$

Ω_{BZ} is the volume of the Brillouin zone, ϵ is the electronic dielectric function, $\omega^{\mathrm{pl}}_{\mathbf{q}}$ is the plasmon energy, and the dipole matrix elements are given by $M_{\mathbf{G}}(\mathbf{k},\mathbf{q}) = \langle\psi_{m\mathbf{k}+\mathbf{q}}|e^{i(\mathbf{q}+\mathbf{G})\cdot\mathbf{r}}|\psi_{n\mathbf{k}}\rangle$. $\psi_{n\mathbf{k}}$ are the Kohn-Sham single-particle orbitals, and Hartree atomic units are used. In order to evaluate Eq. (C1) for n-doped MoS_2, we note the derivative of the dielectric function, which can be expressed as [26]

$$\left[\left.\frac{\partial\epsilon}{\partial\omega}\right|_{\omega^{\mathrm{pl}}_{\mathbf{q}}}\right]^{-1} = -\frac{\omega^{\mathrm{pl}}_{\mathbf{q}}}{2}[\epsilon^{\mathrm{D}}(\mathbf{q},0)^{-1} - \epsilon^{\mathrm{U}}(\mathbf{q},0)^{-1}]. \tag{C2}$$

Here, ϵ^{U} is the static dielectric function of the undoped system, whereas ϵ^{D} is the static dielectric function in the presence of doping-induced free carriers. Owing to the parabolic dispersion of the conduction-band bottom, the energy/momentum dispersion of extrinsic n-type carriers in MoS_2 can be approximated by that of a 2D homogeneous electron gas (2DEG). Correspondingly, the dielectric function of a doped 2D semiconductor can be approximately expressed as

$$\begin{aligned}\epsilon^{\mathrm{D}}(\mathbf{q},\omega=0) &= 1 - v(\mathbf{q})[\chi^{\mathrm{U}}(\mathbf{q}) + \chi^{\mathrm{2DEG}}(\mathbf{q})] \\ &= \epsilon^{\mathrm{U}}_{\infty} + \epsilon^{\mathrm{2DEG}}(\mathbf{q}) - 1,\end{aligned} \tag{C3}$$

where χ denotes the static polarizability, which for a 2DEG can be evaluated analytically [53]. $\epsilon^{\mathrm{U}}_{\infty}$ is the high-frequency dielectric constant, and $\epsilon^{\mathrm{2DEG}}(\mathbf{q}) = 1 - v(\mathbf{q})\chi^{\mathrm{2DEG}}(\mathbf{q})$. By combining Eqs. (C1)–(C3), one can express the electron-plasmon coupling matrix elements of a 2D doped semiconductor as

$$g^{\mathrm{e-pl}}_{mn}(\mathbf{k},\mathbf{q}) = \left(\frac{8\pi}{\omega^{\mathrm{pl}}_{\mathbf{q}}\Omega_{\mathrm{BZ}}}\right)^{\frac{1}{2}} \times \left[\frac{1}{\epsilon^{\mathrm{U}}_{\infty}} - \frac{1}{\epsilon^{\mathrm{U}}_{\infty} + \epsilon^{\mathrm{2DEG}}(\mathbf{q}) - 1}\right]^{-\frac{1}{2}} \frac{M_{\mathbf{G}=0}(\mathbf{k},\mathbf{q})}{|\mathbf{q}|}. \tag{C4}$$

These coupling matrix elements are employed in the calculation of the self-energy due to the electron-plasmon interaction based on the ordinary formalism of the electron-boson interaction [26,42,66,67].

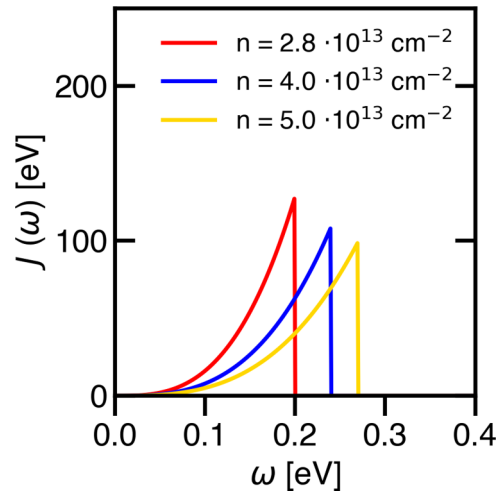

FIG. 10. Density of states for two-dimensional plasmons evaluated from Eq. (D3) for the three carrier concentrations adopted in this work.

APPENDIX D: DENSITY OF STATES OF TWO-DIMENSIONAL PLASMONS

We defined the density of states of 2D plasmons as

$$J(\omega) = {\Omega_{\mathrm{BZ}}}^{-1} \int_{\Omega_{\mathrm{BZ}}} d\mathbf{q}\,\delta\left(\omega - \omega^{\mathrm{pl}}_{\mathbf{q}}\right). \tag{D1}$$

Here, $\omega^{\mathrm{pl}}_{\mathbf{q}}$ is the plasmon frequency, Ω_{BZ} is the area of the 2D Brillouin zone, and the integral extends over Ω_{BZ}. Below, we consider the leading order in q of the plasmon energy in the long-wavelength limit ($\mathbf{q}\to 0$), namely, $\omega^{\mathrm{pl}}_{\mathbf{q}} \simeq \sqrt{2\pi nq/m^*\epsilon^{\mathrm{S}}_{\infty}}$. For isotropic systems, the 2D momentum integral can be expressed as

$$J(\omega) = {\Omega_{\mathrm{BZ}}}^{-1} \int_0^{q_{\mathrm{c}}} dq\, 2\pi q\, \delta(\omega - \alpha\sqrt{q}), \tag{D2}$$

where the integral extends up to the critical momentum q_{c} that marks the onset of Landau damping and we defined $\alpha = \sqrt{2\pi n/m^*\epsilon^{\mathrm{S}}_{\infty}}$. Finally, through a straightforward change in variable and making use of the property of the Dirac δ function $\delta(ax) = |a|^{-1}\delta(x)$, we obtain

$$J(\omega) = {\Omega_{\mathrm{BZ}}}^{-1} \int_0^{\sqrt{q_{\mathrm{c}}}} dx\, \frac{4\pi x^3}{\alpha}\, \delta(x - \omega/\alpha) = \kappa\omega^3\theta(\omega - \omega_{\mathrm{c}}). \tag{D3}$$

For n_1, n_2, and n_3, the density of states is illustrated in Fig. 10.

[1] K. F. Mak, C. Lee, J. Hone, J. Shan, and T. F. Heinz, Atomically Thin MoS_2: A New Direct-Gap Semiconductor, Phys. Rev. Lett. **105**, 136805 (2010).

[2] D. Y. Qiu, F. H. da Jornada, and S. G. Louie, Optical Spectrum of MoS_2: Many-Body Effects and Diversity of Exciton States, Phys. Rev. Lett. **111**, 216805 (2013).

[3] A. Molina-Sánchez, M. Palummo, A. Marini, and L. Wirtz, Temperature-dependent excitonic effects in the optical properties of single-layer MoS_2, Phys. Rev. B **93**, 155435 (2016).

[4] J. Hong, R. Senga, T. Pichler, and K. Suenaga, Probing Exciton Dispersions of Freestanding Monolayer WSe_2 by

Momentum-Resolved Electron Energy-Loss Spectroscopy, Phys. Rev. Lett. **124**, 087401 (2020).

[5] K. F. Mak, K. He, C. Lee, G. H. Lee, J. Hone, T. F. Heinz, and J. Shan, Tightly bound trions in monolayer MoS_2, Nat. Mater. **12**, 207 (2013).

[6] M. Kang, S. W. Jung, W. J. Shin, Y. Sohn, S. H. Ryu, T. K. Kim, M. Hoesch, and K. S. Kim, Holstein polaron in a valley-degenerate two-dimensional semiconductor, Nat. Mater. **17**, 676 (2018).

[7] P. Garcia-Goiricelaya, J. Lafuente-Bartolome, I. G. Gurtubay, and A. Eiguren, Long-living carriers in a strong electron-phonon interacting two-dimensional doped semiconductor, Commun. Phys. **2**, 81 (2019).

[8] D. Zheng, S. Zhang, Q. Deng, M. Kang, P. Nordlander, and H. Xu, Manipulating coherent plasmon-exciton interaction in a single silver nanorod on monolayer WSe_2, Nano Lett. **17**, 3809 (2017).

[9] M. Stührenberg, B. Munkhbat, D. G. Baranov, J. Cuadra, A. B. Yankovich, T. J. Antosiewicz, E. Olsson, and T. Shegai, Strong light-matter coupling between plasmons in individual gold bi-pyramids and excitons in mono- and multilayer WSe_2, Nano Lett. **18**, 5938 (2018).

[10] P. A. D. Gonçalves, L. P. Bertelsen, S. Xiao, and N. A. Mortensen, Plasmon-exciton polaritons in two-dimensional semiconductor/metal interfaces, Phys. Rev. B **97**, 041402(R) (2018).

[11] W. Liu, Y. Wang, C. H. Naylor, B. Lee, B. Zheng, G. Liu, A. T. C. Johnson, A. Pan, and R. Agarwal, Understanding the different exciton-plasmon coupling regimes in two-dimensional semiconductors coupled with plasmonic lattices: A combined experimental and unified equation of motion approach, ACS Photonics **5**, 192 (2018).

[12] J. Cuadra, D. G. Baranov, M. Wersll, R. Verre, T. J. Antosiewicz, and T. Shegai, Observation of tunable charged exciton polaritons in hybrid monolayer WS_2-plasmonic nanoantenna system, Nano Lett. **18**, 1777 (2018).

[13] D. Costanzo, S. Jo, H. Berger, and A. F. Morpurgo, Gate-induced superconductivity in atomically thin MoS_2 crystals, Nat. Nanotechnol. **11**, 339 (2016).

[14] S. Latini, E. Ronca, U. De Giovannini, H. Hbener, and A. Rubio, Cavity control of excitons in two-dimensional materials, Nano Lett. **19**, 3473 (2019).

[15] T. Cao, G. Wang, W. Han, H. Ye, C. Zhu, J. Shi, Q. Niu, P. Tan, E. Wang, B. Liu, and J. Feng, Valley-selective circular dichroism of monolayer molybdenum disulphide, Nat. Commun. **3**, 887 (2012).

[16] H. Beyer, G. Rohde, A. Grubišić Čabo, A. Stange, T. Jacobsen, L. Bignardi, D. Lizzit, P. Lacovig, C. E. Sanders, S. Lizzit, K. Rossnagel, P. Hofmann, and M. Bauer, 80% Valley Polarization of Free Carriers in Singly Oriented Single-Layer WS_2 on Au(111), Phys. Rev. Lett. **123**, 236802 (2019).

[17] K. Kang, S. Xie, L. Huang, Y. Han, P. Y. Huang, K. F. Mak, C.-J. Kim, D. Muller, and J. Park, High-mobility three-atom-thick semiconducting films with wafer-scale homogeneity, Nature (London) **520**, 656 (2015).

[18] N. Briggs *et al.*, Atomically thin half-van der Waals metals enabled by confinement heteroepitaxy, Nat. Mater. **19**, 637 (2020).

[19] S. Moser, L. Moreschini, J. Jaćimović, O. S. Barišić, H. Berger, A. Magrez, Y. J. Chang, K. S. Kim, A. Bostwick, E. Rotenberg, L. Forró, and M. Grioni, Tunable Polaronic Conduction in Anatase TiO_2, Phys. Rev. Lett. **110**, 196403 (2013).

[20] Z. Wang, S. M. Walker, A. Tamai, Y. Wang, Z. Ristic, F. Y. Bruno, A. de la Torre, S. Riccò, N. C. Plumb, M. Shi *et al.*, Tailoring the nature and strength of electron-phonon interactions in the $SrTiO_3$(001) two-dimensional electron liquid, Nat. Mater. **15**, 835 (2016).

[21] A. Janotti, J. B. Varley, M. Choi, and C. G. Van de Walle, Vacancies and small polarons in $SrTiO_3$, Phys. Rev. B **90**, 085202 (2014).

[22] C. Verdi, F. Caruso, and F. Giustino, Origin of the crossover from polarons to Fermi liquids in transition metal oxides, Nat. Commun. **8**, 15769 (2017).

[23] P. G. Moses, A. Janotti, C. Franchini, G. Kresse, and C. G. Van de Walle, Donor defects and small polarons on the TiO_2(110) surface, J. Appl. Phys. **119**, 181503 (2016).

[24] C. Chen, J. Avila, S. Wang, Y. Wang, M. Mucha-Kruczyski, C. Shen, R. Yang, B. Nosarzewski, T. P. Devereaux, G. Zhang, and M. C. Asensio, Emergence of interfacial polarons from electron-phonon coupling in graphene/h-BN van der Waals heterostructures, Nano Lett. **18**, 1082 (2018).

[25] J. M. Riley, F. Caruso, C. Verdi, L. B. Duffy, M. D. Watson, L. Bawden, K. Volckaert, G. van der Laan, T. Hesjedal, M. Hoesch, F. Giustino, and P. D. C. King, Crossover from lattice to plasmonic polarons of a spin-polarised electron gas in ferromagnetic EuO, Nat. Commun. **9**, 2305 (2018).

[26] F. Caruso, C. Verdi, S. Poncé, and F. Giustino, Electron-plasmon and electron-phonon satellites in the angle-resolved photoelectron spectra of *n*-doped anatase TiO_2, Phys. Rev. B **97**, 165113 (2018).

[27] W. H. Sio, C. Verdi, S. Poncé, and F. Giustino, Polarons from First Principles, Without Supercells, Phys. Rev. Lett. **122**, 246403 (2019).

[28] W. H. Sio, C. Verdi, S. Poncé, and F. Giustino, *Ab initio* theory of polarons: Formalism and applications, Phys. Rev. B **99**, 235139 (2019).

[29] P. Amsalem, J. Ma, T. Schultz, F. Caruso, D. Shin, A. Aljarb, E. Longhi, S. Barlow, S. R. Marder, C. Draxl, V. Tung, S. Park, and N. Koch (unpublished).

[30] A. Aljarb, Z. Cao, H.-L. Tang, J.-K. Huang, M. Li, W. Hu, L. Cavallo, and L.-J. Li, Substrate lattice-guided seed formation controls the orientation of 2D transition-metal dichalcogenides, ACS Nano **11**, 9215 (2017).

[31] B. W. H. Baugher, H. O. H. Churchill, Y. Yang, and P. Jarillo-Herrero, Intrinsic electronic transport properties of high-quality monolayer and bilayer MoS_2, Nano Lett. **13**, 4212 (2013).

[32] S. Park, T. Schultz, A. Han, A. Aljarb, X. Xu, P. Beyer, A. Opitz, R. Ovsyannikov, L.-J. Li, M. Meissner, T. Yamaguchi, S. Kera, P. Amsalem, and N. Koch, Electronic band dispersion determination in azimuthally disordered transition-metal dichalcogenide monolayers, Commun. Phys. **2**, 68 (2019).

[33] B. Schuler, D. Y. Qiu, S. Refaely-Abramson, C. Kastl, C. T. Chen, S. Barja, R. J. Koch, D. F. Ogletree, S. Aloni, A. M. Schwartzberg, J. B. Neaton, S. G. Louie, and A. Weber-Bargioni, Large Spin-Orbit Splitting of Deep in-Gap Defect States of Engineered Sulfur Vacancies in Monolayer WS_2, Phys. Rev. Lett. **123**, 076801 (2019).

[34] M. Liu, J. Shi, Y. Li, X. Zhou, D. Ma, Y. Qi, Y. Zhang, and Z. Liu, Temperature-triggered sulfur vacancy evolution in

monolayer MoS_2/graphene heterostructures, Small **13**, 1602967 (2017).

[35] V. Popescu and A. Zunger, Extracting E versus $\vec{k}$ effective band structure from supercell calculations on alloys and impurities, Phys. Rev. B **85**, 085201 (2012).

[36] M. Zacharias and F. Giustino, Theory of the special displacement method for electronic structure calculations at finite temperature, Phys. Rev. Research **2**, 013357 (2020).

[37] T. Eknapakul, P. D. C. King, M. Asakawa, P. Buaphet, R.-H. He, S.-K. Mo, H. Takagi, K. M. Shen, F. Baumberger, T. Sasagawa, S. Jungthawan, and W. Meevasana, Electronic structure of a quasi-freestanding MoS_2 monolayer, Nano Lett. **14**, 1312 (2014).

[38] H. Peelaers and C. G. Van de Walle, Effects of strain on band structure and effective masses in MoS_2, Phys. Rev. B **86**, 241401(R) (2012).

[39] Y. Cai, G. Zhang, and Y.-W. Zhang, Polarity-reversed robust carrier mobility in monolayer MoS_2 nanoribbons, J. Am. Chem. Soc. **136**, 6269 (2014).

[40] W. S. Yun, S. W. Han, S. C. Hong, I. G. Kim, and J. D. Lee, Thickness and strain effects on electronic structures of transition metal dichalcogenides: 2H-MX_2 semiconductors (M = Mo, W; X = S, Se, Te), Phys. Rev. B **85**, 033305 (2012).

[41] H. J. Conley, B. Wang, J. I. Ziegler, R. F. Haglund, S. T. Pantelides, and K. I. Bolotin, Bandgap engineering of strained monolayer and bilayer Mo_2, Nano Lett. **13**, 3626 (2013).

[42] F. Giustino, Electron-phonon interactions from first principles, Rev. Mod. Phys. **89**, 015003 (2017).

[43] G. Anemone, A. A. Taleb, G. Benedek, A. Castellanos-Gomez, and D. Faras, Electron-phonon coupling constant of 2H-MoS_2(0001) from helium-atom scattering, J. Phys. Chem. C **123**, 3682 (2019).

[44] M. R. Filip, C. Verdi, and F. Giustino, GW band structures and carrier effective masses of $CH_3NH_3PbI_3$ and hypothetical perovskites of the type $APbI_3$: A = NH_4, PH_4, AsH_4, and SbH_4, J. Phys. Chem. C **119**, 25209 (2015).

[45] S. Poncé, E. R. Margine, and F. Giustino, Towards predictive many-body calculations of phonon-limited carrier mobilities in semiconductors, Phys. Rev. B **97**, 121201(R) (2018).

[46] O. Anderson, Deconvolution of UPS and XPS spectra, Vacuum **41**, 1700 (1990).

[47] A. Molina-Sánchez and L. Wirtz, Phonons in single-layer and few-layer MoS_2 and WS_2, Phys. Rev. B **84**, 155413 (2011).

[48] N. F. Mott, Metal-insulator transition, Rev. Mod. Phys. **40**, 677 (1968).

[49] B. Radisavljevic and A. Kis, Mobility engineering and a metal-insulator transition in monolayer MoS_2, Nat. Mater. **12**, 815 (2013).

[50] F. Caruso and F. Giustino, The GW plus cumulant method and plasmonic polarons: Application to the homogeneous electron gas, Eur. Phys. J. B **89**, 238 (2016).

[51] F. Caruso, D. Novko, and C. Draxl, Phonon-assisted damping of plasmons in three- and two-dimensional metals, Phys. Rev. B **97**, 205118 (2018).

[52] J. Fontanella, C. Andeen, and D. Schuele, Low-frequency dielectric constants of alpha-quartz, sapphire, MgF_2, and MgO, J. Appl. Phys. **45**, 2852 (1974).

[53] G. F. Giuliani and G. Vignale, *Quantum Theory of the Electron Liquid* (Cambridge University Press, Cambridge, 2005).

[54] D. C. Langreth, Singularities in the x-ray spectra of metals, Phys. Rev. B **1**, 471 (1970).

[55] F. Aryasetiawan, L. Hedin, and K. Karlsson, Multiple Plasmon Satellites in Na and Al Spectral Functions from *Ab Initio* Cumulant Expansion, Phys. Rev. Lett. **77**, 2268 (1996).

[56] M. Guzzo, G. Lani, F. Sottile, P. Romaniello, M. Gatti, J. J. Kas, J. J. Rehr, M. G. Silly, F. Sirotti, and L. Reining, Valence electron Photoemission Spectrum of Semiconductors: *Ab Initio* Description of Multiple Satellites, Phys. Rev. Lett. **107**, 166401 (2011).

[57] F. Caruso, H. Lambert, and F. Giustino, Band Structures of Plasmonic Polarons, Phys. Rev. Lett. **114**, 146404 (2015).

[58] F. Caruso and F. Giustino, Spectral fingerprints of electron-plasmon coupling, Phys. Rev. B **92**, 045123 (2015).

[59] B. Gumhalter, V. Kovač, F. Caruso, H. Lambert, and F. Giustino, On the combined use of *GW* approximation and cumulant expansion in the calculations of quasiparticle spectra: The paradigm of Si valence bands, Phys. Rev. B **94**, 035103 (2016).

[60] F. Caruso, C. Verdi, and F. Giustino, Many-body calculations of plasmon and phonon satellites in angle-resolved photoelectron spectra using the cumulant expansion approach, *Handbook of Materials Modeling* (Springer, Berlin, 2018) pp. 1–25.

[61] Ground-state electronic structure calculations were conducted with density functional theory as implemented in QUANTUM ESPRESSO [68]. We used Troullier-Martin norm-conserving pseudopotentials and the Perdew-Burke-Ernzerhof (PBE) approximation to the exchange-correlation functional. We used the PBE-relax crystal structure, a 100 Ry kinetic energy cutoff, and a $10 \times 10 \times 1\mathbf{k}$-point grid. Spin-orbit coupling effects do not influence the energy dispersion of the CBM [69]. The electron-plasmon self-energy was computed with the EPW code [67] by interpolating the electronic band energies on a random grid of $2 \times 10^6\mathbf{k}$ points using maximally localized Wannier functions [70,71], and plasmons energies were extracted from plasmon dispersion.

[62] Ground-state electronic structure calculations were conducted with density functional theory as implemented in QUANTUM ESPRESSO [68]. We used Troullier-Martin norm-conserving pseudopotentials and the Perdew-Burke-Ernzerhof (PBE) approximation to the exchange-correlation functional. We used the PBE-relax crystal structure, a 100 Ry kinetic energy cutoff, and a $10 \times 10 \times 1\mathbf{k}$-point grid. Spin-orbit coupling effects do not influence the energy dispersion of the CBM [69]. The electron-plasmon self-energy was computed with the EPW code [67] by interpolating the electronic band energies on a random grid of $2 \times 10^6\mathbf{k}$ points using maximally localized Wannier functions [70,71], and plasmons energies were extracted from plasmon dispersion.

[63] http://en.uhem.itu.edu.tr/

[64] P. V. C. Medeiros, S. Stafström, and J. Björk, Effects of extrinsic and intrinsic perturbations on the electronic structure of graphene: Retaining an effective primitive cell band structure by band unfolding, Phys. Rev. B **89**, 041407(R) (2014).

[65] D. Pines and J. R. Schrieffer, Approach to equilibrium of electrons, plasmons, and phonons in quantum and classical plasmas, Phys. Rev. **125**, 804 (1962).

[66] F. Caruso and F. Giustino, Theory of electron-plasmon coupling in semiconductors, Phys. Rev. B **94**, 115208 (2016).

[67] S. Poncé, E. Margine, C. Verdi, and F. Giustino, EPW: Electron-phonon coupling, transport and superconducting properties using maximally localized Wannier functions, Comput. Phys. Commun. **209**, 116 (2016).

[68] P. Giannozzi *et al.*, Advanced capabilities for materials modelling with Quantum ESPRESSO, J. Phys.: Condens. Matter **29**, 465901 (2017).

[69] A. Molina-Sánchez, D. Sangalli, K. Hummer, A. Marini, and L. Wirtz, Effect of spin-orbit interaction on the optical spectra of single-layer, double-layer, and bulk MoS_2, Phys. Rev. B **88**, 045412 (2013).

[70] A. A. Mostofi, J. R. Yates, Y.-S. Lee, I. Souza, D. Vanderbilt, and N. Marzari, wannier90: A tool for obtaining maximally-localised Wannier functions, Comput. Phys. Commun. **178**, 685 (2008).

[71] N. Marzari, A. A. Mostofi, J. R. Yates, I. Souza, and D. Vanderbilt, Maximally localized Wannier functions: Theory and applications, Rev. Mod. Phys. **84**, 1419 (2012).